Selective Deposition of Cobalt and Copper Oxides on BiVO 4 Facets for Enhancement of CO 2 Photocatalytic Reduction to Hydrocarbons

Xiang Yu, Vitaly Ordomsky, Andrei Khodakov

Heterogeneous & Homogeneous & Bio- & Nano-

CHEMCATCHEM

CATALYSIS

Accepted Article

Title: Selective deposition of cobalt and copper oxides on BiVO4 facets for enhancement of CO2 photocatalytic reduction to hydrocarbons

Authors: Xiang Yu, Vitaly Ordomsky, and Andrei Khodakov

To be cited as: *ChemCatChem* 10.1002/cctc.201901115

Link to VoR: http://dx.doi.org/10.1002/cctc.201901115

A Journal of

ChemPubSoc Europe

WILEY-VCH

www.chemcatchem.org

Selective deposition of cobalt and copper oxides on $BiVO_4$ facets for enhancement of CO_2 photocatalytic reduction to hydrocarbons

Dr. Xiang Yu[a], Dr. Vitaly V. Ordomsky[a, b] and Dr. Andrei Y. Khodakov[a*]*

[a]Univ. Lille, CNRS, Centrale Lille, ENSCL, Univ. Artois, UMR 8181 - UCCS - Unité de Catalyse et Chimie du Solide, F-59000 Lille, France

[b]Eco-Efficient Products and Processes Laboratory (E2P2L), UMI 3464, CNRS-Solvay, 201108 Shanghai, People's Republic of China

Corresponding authors: vitaly.ordomsky@univ-lille.fr, andrei.khodakov@univ-lille.fr

Abstract

The nanostructure of a semiconductor is a crucial parameter for efficient photocatalytic performance. Hereby, we have synthesized monoclinic bismuth vanadate ($BiVO_4$) crystals with controlled ratio of {010} and {110} facets. The selective deposition of CuO_x and CoO_x over {010} and {110} facets has been performed using photo-reduction and photo-oxidation methods, respectively. It resulted in a highly efficient charge separation of photogenerated electrons and holes and enhancement of the photocatalytic reduction of CO_2 by H_2O into hydrocarbons, including CH_4, C_2H_6 and C_3H_8. The controlled co-catalyst deposition over different semiconductor facets provides a strategy for the synthesis of hydrocarbons from CO_2 and H_2O by efficient charge separation.

1. Introduction

Carbon dioxide is widely recognized as a major greenhouse gas that causes global

environmental problems[1]. Worldwide consumption of limited fossil fuels not only accelerates their depletion but also results in production of excessive atmospheric CO_2. In this regard, transformation of CO_2 to the fuels is a promising method for simultaneous solution of energy and environmental problems[2]. In 1979, Japanese researcher Fujishima and Honda reported [3] for the first time the photocatalytic reduction of CO_2 into organic compounds using semiconductor catalysts such as SiC, GaP, and TiO_2. Since then, numerous works have focused on the development of new semiconductor materials for reduction of CO_2 [4-7]. Various semiconductors were proven to be effective in photocatalytic reduction of CO_2, for example: TiO_2 [8, 9], Ga_2O_3 [10, 11], Zn_2GeO_4 [12, 13], WO_3 [14], Bi_2WO_6 [15, 16] and so on. The main products of photocatalytic reduction of CO_2 by water are usually methane, higher hydrocarbons, methanol, ethanol, formaldehyde, formic acid or CO [7].

Although a lot of progress has been made in this field, the activity of photocatalytic reduction of CO_2 is still insufficient due to poor charge separation and low quantum efficiency. In addition, photocatalytic transformation of CO_2 is limited due to low adsorption over the catalyst and difficulties in the activation of the stable CO_2 molecule.

In the photocatalytic reaction, the difference in the morphology of the catalyst often has a significant impact on the photocatalytic performance [17]. The difference in catalyst morphology is mainly reflected by the exposure of different crystal facets, or the proportion of exposed crystal facets. In recent years, more and more reports have addressed the effects of exposed crystals on photocatalytic properties. It is generally believed that photocatalysts exhibit better catalytic properties when more active crystal facets are exposed to reacting molecules [18, 19]. In many classical photocatalytic semiconductors, it has been shown that

controlling the exposure of a suitable crystal facets is an effective strategy to improve photocatalytic performance, for example: TiO_2 [20, 21], $BiVO_4$ [22-24], Cu_2O [25, 26] and CeO_2 [27]. In photocatalytic reactions, the high recombination rate of photogenerated electrons and holes is a major factor limiting its photocatalytic performance. The recombination rate of photogenerated electrons and holes can be greatly reduced with increase of activity by deposition of co-catalysts over semiconductors. In general, the role of co-catalyst can be relevant to the following processes: (1) better charge separation, (2) higher activity and selectivity of CO_2 reduction by suppression of side reactions and (3) enhanced stability of photocatalyst [28].

Bismuth vanadate ($BiVO_4$) is a promising visible light-driven semiconductor photocatalyst with low production cost, low toxicity, high stability and narrow band gap (2.4 eV) with good response to visible light excitation. $BiVO_4$ has demonstrated as efficient catalyst for the reduction of CO_2 into methanol and ethanol [29, 30]. However, the photocatalytic efficiency of $BiVO_4$ is low because of relatively low visible-light utilization and inefficient charge separation. The formation of Z-scheme photocatalytic systems that mimic natural photosynthesis with photocatalytic systems and electron mediator is a promising strategy to improve charge separation [31]. According to a few reports, the photocatalytic efficiency can be improved by Z-scheme on the $BiVO_4$ catalyst [32-34].

Herein, the separation of electrons and holes in bismuth vanadate ($BiVO_4$) is improved by control of the semiconductor morphology. The photocatalytic reduction of CO_2 under irradiation is significantly enhanced by selective photo-deposition of Cu and Co co-catalysts over different facets providing Z-scheme charge flow.

2. Experimental

2.1 Synthesis of monoclinic $BiVO_4$ crystal with controllable exposed facets

Monoclinic $BiVO_4$ crystal was synthesized by a hydrothermal method. In brief, the precursors NH_4VO_3 (0.015 mol) and $Bi(NO_3)_3 \cdot 5H_2O$ (0.015 mol) were dissolved in an aqueous nitric acid solutions (2 M), and the pH value of the solution was adjusted to 2.0 with ammonia solution (14.84 M) under continuous stirring. An orange precipitate appears over time. After that, NaCl was added into the suspension and stirring was continued for 30 minutes. After about 5 h aging, the suspension was transferred to a Teflon-lined stainless steel autoclave with a capacity of 100 mL and treated under hydrothermal conditions at 473 K for 24 h. After the autoclave was cooled down to room temperature, the yellow powdery sample was separated by filtration, washed with deionized water for several times, and then dried at 353 K in air for overnight. Finally, the sample was calcined at 773 K in air for 2 h. The samples were denoted as $BiVO_4$-x M, and x represents the concentration of NaCl in the suspension.

2.2 Synthesis of monoclinic $BiVO_4$ crystal with predominantly exposed {010} and {110} facets

Synthesis of $BiVO_4$-010

The precursor $Bi(NO_3)_3 \cdot 5H_2O$ (0.015 mol) was dissolved into an aqueous nitric acid solutions (4 M). And the precursors NH_4VO_3 (0.015 mol) was dissolved into another aqueous sodium hydroxide solution (2 M). Afterwards, sodium dodecyl benzene sulfonate (0.002 mol) was added to the above solutions separately. After stirring for 30 minutes, the above two solutions were mixed under continuous stirring. The pH value of mixed solutions was adjusted to 7.0 with sodium hydroxide solution (2 M). After about 1 h stirring, the mixed solution was

transferred into Teflon-lined stainless steel autoclave and hydrothermally treated at 473 K for 1.5 h. The yellow powdery was recovered by filtration, washed with deionized water for several times, and then dried at 353 K in air for overnight. This sample was denoted as $BiVO_4$-010.

Synthesis of $BiVO_4$-110

The $BiVO_4$-110 sample was synthesized using solid-liquid state reaction by mixing equal amount of Bi_2O_3 (0.005 mol) and V_2O_5 (0.005 mol) in an aqueous nitric acid solution (1 M). The suspension was stirred for four days at room temperature. The yellow powdery was separated by filtration, washed with deionized water for several times and dried at 353 K in air for overnight. This sample was denoted as $BiVO_4$-110.

2.3 Selective photo-deposition of metal oxides in monoclinic $BiVO_4$ crystal

Photo-reduction and photo-oxidation procedures have been used for deposition of co-catalysts. 1.0 g $BiVO_4$ powder and a calculated amount of metal precursors were added in 40 mL deionized water containing a sacrificial agent. After about 20 minutes ultrasonic dispersion, the aqueous suspension under irradiation with a 300 W Xe lamp for 5 h under continuous stirring with the protection of nitrogen. Then the suspension was filtered, washed with deionized water for several times and dried at 353 K in air for overnight.

5 wt% of metal in the form of metal oxides (WO_x, FeO_x, ZnO_x, CuO_x and CoO_x) were deposited over $BiVO_4$-0.20M by photo-reduction procedure using 20 wt% of methanol as sacrificial agent and $(NH_4)_{10}(H_2W_{12}O_{42})\cdot 4H_2O$, $Fe(NO_3)_3\cdot 9H_2O$, $Zn(NO_3)_2\cdot 6H_2O$ and $Cu(NO_3)_2\cdot 3H_2O$ as precursors, respectively. The obtained samples were denoted as **WO_x/$BiVO_4$**, **FeO_x/$BiVO_4$**, **ZnO_x/$BiVO_4$** and **CuO_x/$BiVO_4$**.

5 wt% of metal in the form of metal oxides MnO_x, PbO_2 and CoO_x have been deposited over $CuO_x/BiVO_4$ by photo-oxidation technique using $NaIO_3$ (0.1 M) as the electron acceptor and $Mn(NO_3)_2 \cdot xH_2O$, $Pd(NO_3)_2 \cdot xH_2O$ and $Co(NO_3)_3 \cdot 6H_2O$ as precursor, respectively. The obtained samples were denoted as **$MnO_x/CuO_x/BiVO_4$**, **$PbO_2/CuO_x/BiVO_4$** and **$CoO_x/CuO_x/BiVO_4$**.

For comparison, the reference sample **$CoO_x/CuO_x/BiVO_4$(imp)** has been synthesized by impregnation of $Cu(NO_3)_2 \cdot 3H_2O$ and $Co(NO_3)_3 \cdot 6H_2O$ over $BiVO_4$-0.20M with subsequent calcination at 673 K.

2.4 Characterization.

The X-ray powder diffraction (XRD) experiments were conducted using a Bruker AXS D8 diffractometer with Cu Kα radiation (λ = 0.1538 nm). The XRD patterns were collected in the 5−80° (2θ) range. The diffuse reflectance UV-visible spectra of the catalysts were recorded on a Perkin-Elmer Lambda 650 S UV/VIS spectrometer equipped with an integrating sphere covered with $BaSO_4$ as a reference.

The textural properties of the samples were studied by N_2 physisorption on a Micromeritics Tristar 3020 apparatus.

The photoluminescence spectroscopy measurements were performed on a LabRam HR (Horiba scientific). For excitation, 532 nm radiation from a diode-pumped solid-state 300 μW laser was used. The spectrophotometer has an entrance slit of 100 μm, and is equipped with a 300 lines/mm^{-1} grating that permits to achieve a spectral resolution of 3.8 cm^{-1} per pixel. The luminescence light was detected with a CCD camera operating at 138 K.

The SEM measurements were carried out using JEOL scanning electron microscope with 30 Kv accelerating voltage.

The XPS spectra were registered using a Kratos Axis spectrometer, equipped with an aluminum monochromater for a 1486.6 eV source working at 120 W. All spectra were recorded under a vacuum of 10^{-8} Torr and recalibrated afterwards with the binding energy of the Al 2p at 74.6 eV.

2.5 Photocatalytic tests

The photocatalytic reduction of CO_2 in water was carried out in a homemade stainless-steel batch reactor (~250 mL) with a quartz window on the top of the reactor. The light source was 400 W Xe lamp (Newport). The catalyst was placed on a quartz glass holder in the middle of reactor (**Figure S1, SI**). 15 ml of liquid water was added at the bottom of reactor. The reaction has been conducted at 323 K and 0.2 MPa of CO_2. Before start of the photocatalytic reaction, the reactor was kept in the dark for 1 h to ensure an adsorption-desorption equilibrium between the photocatalyst and the reactants. Subsequently, the reactor was irradiated by a 400 W Xe lamp. The spectral range of the irradiation was selected using Hamamatsu optical filter. The photocatalytic reaction time was typically 7 h.

The gas phase reaction products (CO, CH_4, C_2H_6 and C_3H_8) were analyzed by on-line gas chromatography (GC, PerkinElmer Clarus® 580). Liquid products such as HCHO and CH_3OH were analyzed by off-line GC analysis. The GC was equipped with a PoraBOND Q and ShinCarbon ST 100/120 columns with detection by flame ionization detector (FID) and a thermal conductivity detector (TCD).

3. Results and discussion

3.1 Monoclinic $BiVO_4$ crystal with designable facets

Uniform truncated tetragonal bipyramidal morphology $BiVO_4$ with designable exposed facets has been prepared using hydrothermal method with variation of NaCl content [24]. XRD measurements indicate that these samples exhibit a monoclinic structure [23, 35] (**Figure 1**). The intensity of the (040) diffraction peak at 30.5 2θ depends on the concentration of NaCl. Increase of NaCl concentration from 0.04 to 0.5 M leads to increase of intensity with subsequent rapid decrease when the concentration reaches 2 M, indicating that NaCl affects the morphology of $BiVO_4$.

The SEM images show that the $BiVO_4$ crystals were composed of uniformed single crystal with truncated tetragonal bipyramidal shape (**Figure 2b-e**) when the concentration of NaCl is between 0.04 - 0.50 M. However, the $BiVO_4$ crystals has an irregular morphology (**Figure 2a,f**) when NaCl was not included or if the concentration is too high. Interestingly, the morphology of monoclinic $BiVO_4$ crystals changed gradually with the concentration of NaCl. Crystal model of monoclinic $BiVO_4$ crystals with truncated tetragonal bipyramidal shape contains two {010} facets on the top and bottom and eight {110} facets on the edges (**Figure 3**). The fraction of {010} facets has been calculated by the crystal model equation. The percentages of {010} facets can be calculated as follows [21, 24].

$S_{010} = 2a^2$,

$S_{110} = 8 * 0.5 * (a + b) * L_{DE}$, $L_{DE} = L_{CE} – L_{CD}$, $L_{CE} = 0.5b / \cos\theta$, $L_{CD} = 0.5a / \cos\theta$,

$S_{110} = 2 * (b^2 – a^2) / \cos\theta$,

$F_{010\%} = S_{110} / (S_{110} + S_{010}) = 2a^2 / 2 * (b^2 – a^2) / \cos\theta = \cos\theta / (\cos\theta + b^2 / a^2 – 1)$

Here θ is the theoretical value (66.07°) for the angle between the {010} and {110} facets of monoclinic $BiVO_4$ crystal. Note that the fraction of {010} facets increases significantly with the increase of NaCl concentration from 26 % to 75 % (**Table 1**).

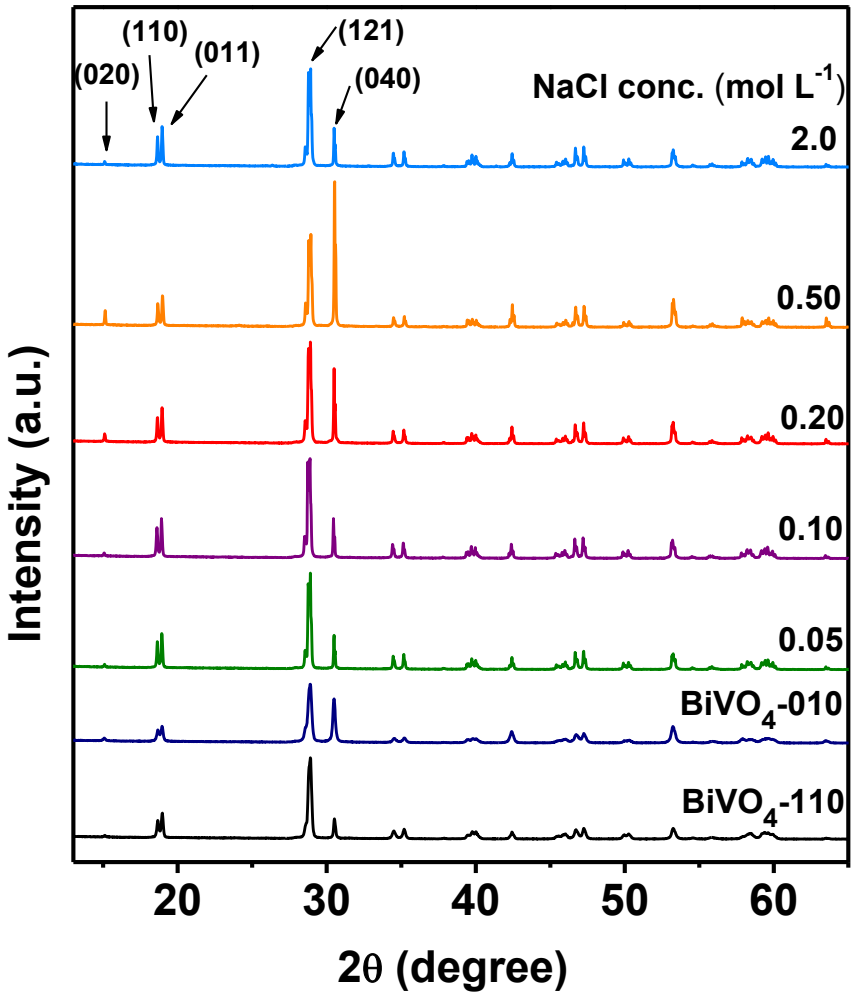

Figure 1. *XRD patterns of the monoclinic $BiVO_4$ samples with different concentration of NaCl and BiVO4 with predominately exposed {010} and {110} facets*

$BiVO_4$-010 and $BiVO_4$-110 samples with predominantly {010} and {110} facets have been synthesized. The SEM images confirm that the $BiVO_4$ crystals have {010} and {110} facets predominantly exposed (**Figure 2**). XRD measurements also confirm synthesis of

$BiVO_4$-010 and $BiVO_4$-110 samples with predominantly {010} and {110} facets (**Figure 1**).

The UV-Vis diffuse reflectance spectra of the $BiVO_4$ crystals with different concentration of NaCl is shown in **Figure 4**. The samples exhibit intense absorption in the ultraviolet region (< 400 nm) as well as visible light region (< 500 nm). The band gap energy for different morphology samples estimated using Tauc's plots of UV-Vis spectra is the same, being 2.3 eV (**Table 1**).

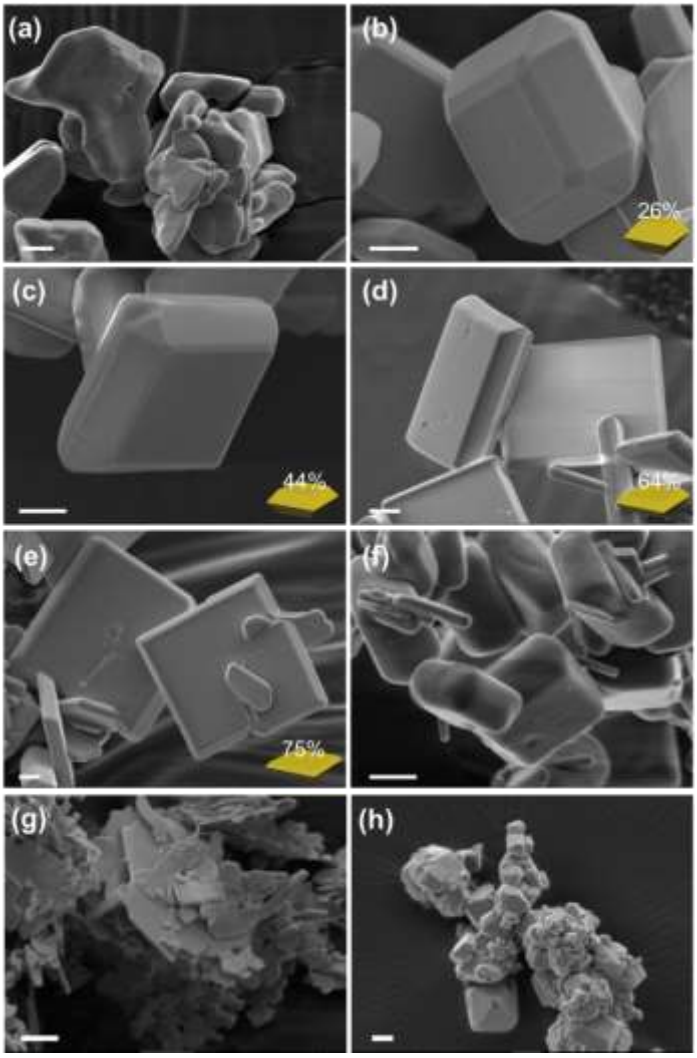

Figure 2. *SEM images of $BiVO_4$ samples synthesized with different concentration of NaCl. NaCl concentration: (a) 0 M, (b) 0.04 M, (c) 0.10 M, (d) 0.20 M, (e) 0.50 M, (f) 2.0 M, (g) BiVO4-010, (h) BiVO4-110. Scale bar: 1.0 μm.*

10.1002/cctc.201901115

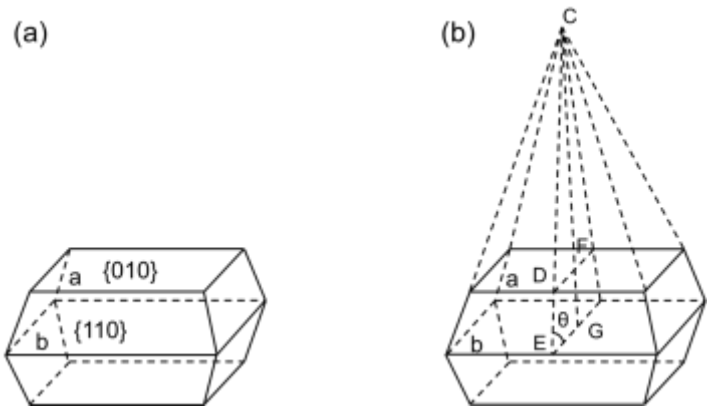

Figure 3. *Crystal model of monoclinic $BiVO_4$ crystals with truncated tetragonal bipyramidal shape.*

Photoluminescence spectroscopy has been used to evaluate the recombination of holes and electrons of different $BiVO_4$ catalysts. A luminescence band centered at 620 nm was observed for monoclinic $BiVO_4$ crystals (**Figure 5**). It is generally accepted that photoluminescence is produced by the recombination of photogenerated carriers on a semiconductor, and therefore the higher intensity of the luminescent band means that the probability of photogenerated carrier recombination is higher [36]. For the series of $BiVO_4$ samples, the intensity of the luminescence band decreases in the order of $BiVO_4$-0.04M > $BiVO_4$-0M > $BiVO_4$-2.0M > $BiVO_4$-0.50M > $BiVO_4$-0.10M > $BiVO_4$-0.20M, indicating that $BiVO_4$-0.20M with 64 % of {010} facet has the lowest ability of electron-hole recombination. Note that the irregular $BiVO_4$ crystals show a higher ability of electron-hole recombination. In other words, truncated tetragonal bipyramidal shape is good for electron-hole separation.

10.1002/cctc.201901115

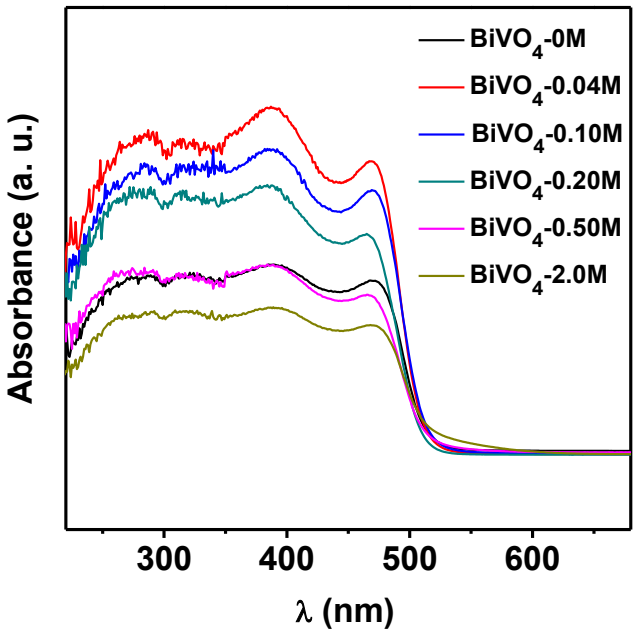

Figure 4. *UV-Vis spectra of $BiVO_4$ samples synthesized with different concentration of NaCl.*

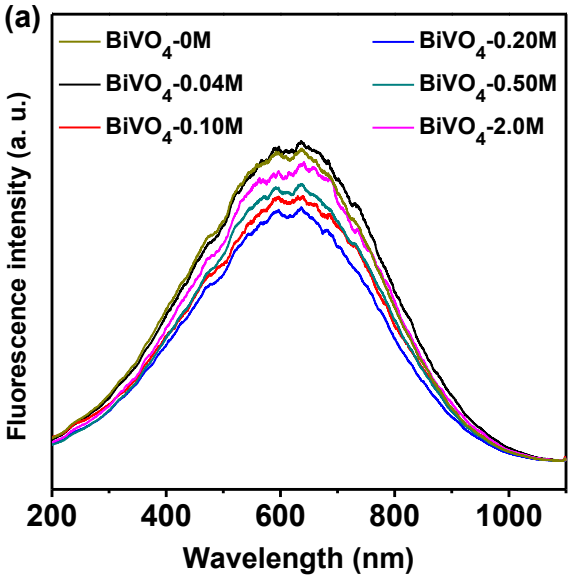

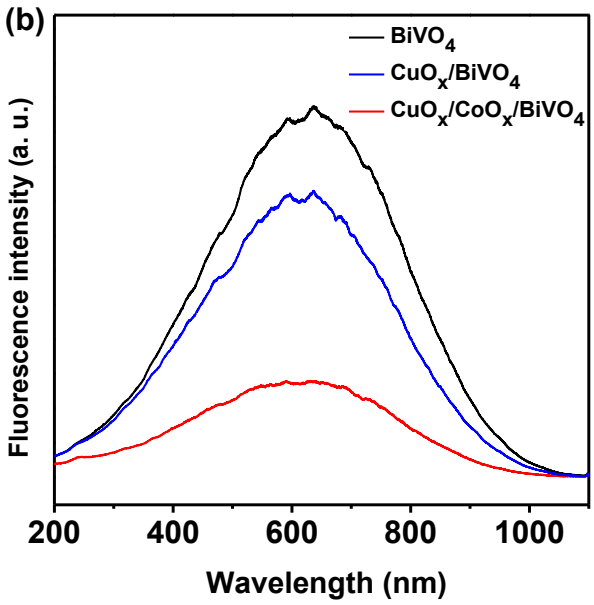

Figure 5. *(a) Photoluminescence spectra of $BiVO_4$ samples synthesized with different concentration of NaCl. (b) Photoluminescence spectra of $BiVO_4$-0.20M crystal with selective photo-deposited the metal oxides.*

The UV-Vis diffuse reflectance spectra (**Figure 6**) of CuO_x/CoO_x /$BiVO_4$-0.20M nanocomposite and reference compounds are displayed in Figure. It is noted that each sample shows different absorption profile in visible light region except for that of strong absorption in the UV-light region. The presence of Co_3O_4 results in an increase in the ability of visible light absorption. Co_3O_4 has absorption in nearly all of the visible light range and induces an extension of the light absorption spectrum of the composite semiconductor even at low cobalt contents. The band gap energy for different nanocomposites was estimated using Tauc's plots of UV-Vis spectra. The direct band gaps of $BiVO_4$, CuO_x/ $BiVO_4$ and CuO_x/CoO_x /$BiVO_4$ samples are estimated to be 2.34, 2.30 and 2.16 eV. They are slightly smaller than the reported values of pure $BiVO_4$. The decrease in band gap energy indicates that the nanocomposite has a much greater optical absorption region than pure $BiVO_4$, which can be excited to produce

more electron–hole pairs under the same visible light illumination and then result in higher photocatalytic activity.

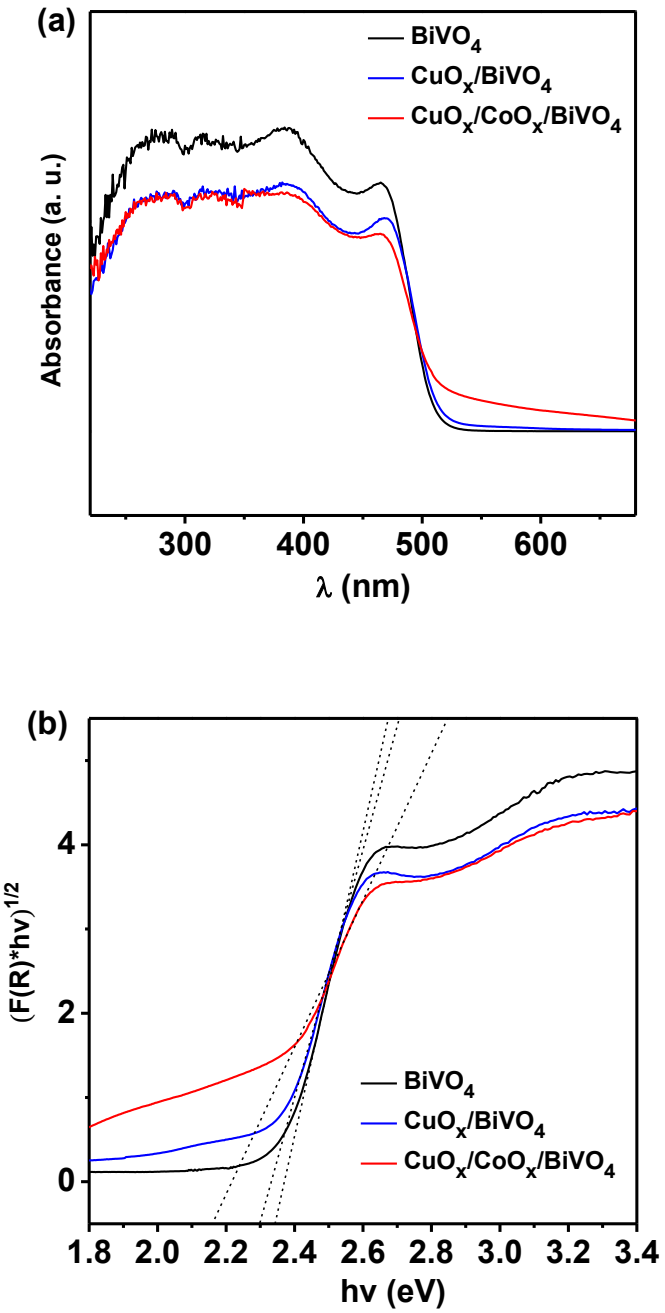

Figure 6 *a. UV-Vis spectra of CuO_x/CoO_x /$BiVO_4$-0.20M sample b. $[F(R\infty)hv]^{1/2}$ versus hv for CuO_x/CoO_x /$BiVO_4$-0.20M sample*

Table 1. *Fraction of {010} facets, specific surface areas, bandgap energies of $BiVO_4$ samples with different NaCl concentration.*

Sample	Fraction of {010} facets (%)	Surface area (m^2 g^{-1})	Bandgap energy (eV)
$BiVO_4$-0M	/	1.3	2.3
$BiVO_4$-0.04M	26	2.2	2.3
$BiVO_4$-0.10M	44	2.8	2.3
$BiVO_4$-0.20M	64	2.9	2.3
$BiVO_4$-0.50M	75	2.6	2.3
$BiVO_4$-2.0M	/	1.4	2.3

ZnO_x, WO_x, FeO_x and CuO_x were loaded onto series of $BiVO_4$ samples through photo-reduction deposition technique (**Figure 7**). SEM images show that CuO_x nanoparticles were selectively deposited onto the {010} facets of $BiVO_4$ crystal (**Figure 8b**). Several oxide co-catalysts MnO_x, PbO_2 and CoO_x have been deposited by photo-oxidation using $NaIO_3$ as sacrificial agent on the surface of $CuO_x/BiVO_4$ catalyst. SEM analysis demonstrates that these oxides are located on the {110} facets of $BiVO_4$ crystal (**Figure 7, 8c**).

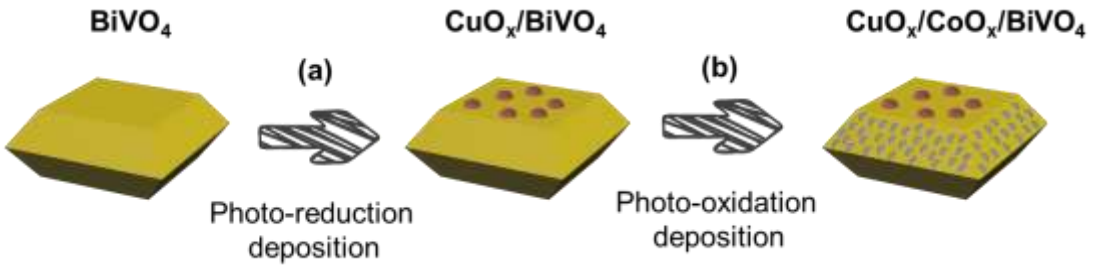

Figure 7. *Schematic of the synthesis of $CuO_x/CoO_x/BiVO_4$ catalyst.*

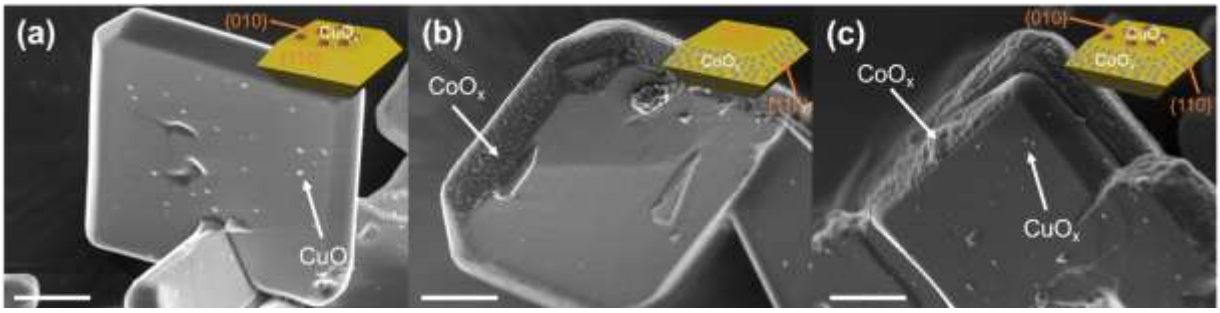

Figure 8. *SEM images of $BiVO_4$-0.20M sample with selective photo-deposited metal oxides: (a) $CuO_x/BiVO_4$, (b) $CoO_x/BiVO_4$, (c) $CuO_x/CoO_x/BiVO_4$.*

To provide further insights into the copper and cobalt state in $CoO_x/CuO_x/BiVO_4$ catalyst was characterized by XPS (**Figure S2, SI**). The binding energies of Cu $2p_{3/2}$ for the catalyst was about 932.7 eV, which could be attributed to either Cu^0 or Cu^I [37-39]. The positions of the Cu L_3VV Auger lines for these samples were centered at 916.7 eV, corresponding to that of Cu^I in Cu_2O [40]. **Figure S2, SI** represents the Co 2p XPS spectra of the catalyst. Co $2p_{3/2}$ binding energies at 781.5 eV, absence of the satellite structure and $2p_{3/2}$-$2p_{1/2}$ spin-orbit splitting (ΔE) of 15.1 eV indicates on the presence of Co_3O_4 phase [41-43].

3.2 Catalytic performance

Figure 9 demonstrates the effect of photo-reductive deposition of different metal oxides over $BiVO_4$-0.20M sample, which according to our characterization study demonstrates the most efficient charge separation. Methane, ethane, propane, formaldehyde and methanol were formed as the products of the reaction of CO_2 reduction by H_2O. The deposition of W and Fe does not lead to significantly improve of the catalytic performance in comparison with the parent $BiVO_4$-0.20M which is almost inactive. The main products of the reaction were CO and methane. In the presence of ZnO_x activity significantly increases to 2 $\mu molg^{-1}h^{-1}$ with increase of the contribution of methane in the products in comparison with CO. The highest

activity (6.8 μmolg^{-1}h^{-1}) has been observed over $CuO_x/BiVO_4$-0.20M with formation of broad range of hydrocarbons (methane, ethane and propane) and oxygenates (formaldehyde and methanol).

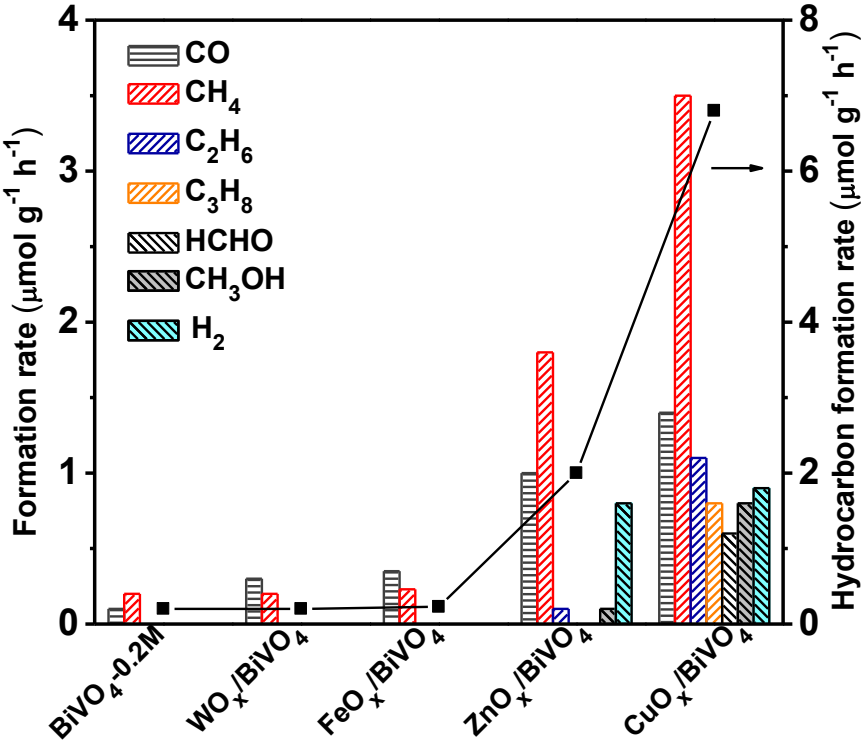

Figure 9. *Effect of metal oxides on the performance of $BiVO_4$-0.20M for photocatalytic reduction CO_2 with H_2O.*

Further we have studied effect of CuO_x deposition over $BiVO_4$ catalyst with systematically changed fraction of {010} facets (**Figure 10**). As compared to $BiVO_4$ with an irregular morphology, which was synthesized without addition of NaCl, $CuO_x/BiVO_4$ catalysts with a uniform truncated tetragonal bipyramidal morphology exhibited higher formation rate of hydrocarbon fuels. Interestingly, the photocatalytic performance depends on the fraction of {010} facets. The formation rate of hydrocarbons has bell shaped curve with

maximum at the fraction of exposed {010} facets 64 % with formation rate 6.8 μmolg^{-1}h^{-1}. CuO_x/$BiVO_4$-010 and CuO_x/$BiVO_4$-110 with predominantly {010} and {110} facets demonstrate lower formation rate of hydrocarbons in comparison with catalysts containing both facets.

Our characterizations clarified that the specific surface areas change slightly with an increase in the fraction of {010} facets. These cannot explain the change in the catalytic behaviours with an increase in the fraction of {010} facets. Furthermore, the bandgap energy values calculated from the UV-vis spectroscopy for this series of catalysts were the same, being 2.3 eV (**Table 1**). Thus, the observation that the $BiVO_4$ single crystal with an 64% fraction of {010} and {110} facets shows the highest catalytic performance (**Table 1**) suggests that both facets play crucial roles in the photocatalytic reduction CO_2.

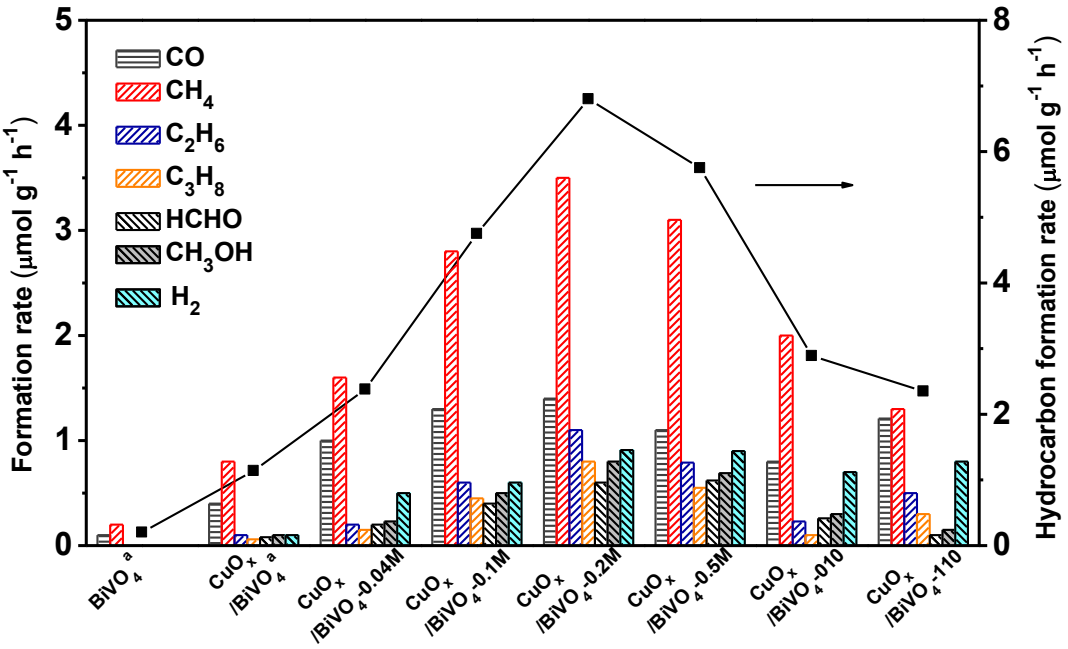

Figure 10. *Effect of the fraction of {010} facets on the photocatalytic performance of CuO_x/$BiVO_4$ catalyst for reduction CO_2 with H_2O. [a] $BiVO_4$ with an irregular morphology (NaCl concentration: 0M).*

Recent studies have demonstrated that photogenerated electrons and holes in monoclinic $BiVO_4$ crystals will migrate to the {010} and {110} facets respectively [23]. Li and coworker [44] evaluated the energy levels of {010} and {110} facets of $BiVO_4$ crystals by DFT calculation method. They observed a slight difference in energy of the valence and conductive band between the {010} and {110} facets which suggested that the electron transfer from {110} to {010} facets is feasible thermodynamically. Thus, it can be expected that the coexistence of the {010} and {110} facets with the appropriate ratio will favor the separation of photogenerated electrons and holes. This order fits well with obtained photoluminescence measurement, confirming that the {010} and {110} facet coexistence and appropriate ratio facilitates the separation of electron-hole pairs. Furthermore, the order of the efficiency of electron-hole pairs separation is the same as that of the formation rate of hydrocarbon fuels for the photocatalytic reduction of CO_2 with H_2O (**Figure 10**). Therefore, we believe that the ability of electron-hole pairs separation is a key factor in determining the catalytic behavior of $CuO_x/BiVO_4$ with different fraction of {010} facets.

Table 2 displays the photocatalytic performance data of $CuO_x/BiVO_4$ with different CuO_x contents over $BiVO_4$-0.20M. Note that the increase in Cu content from 1 to 5 wt% enhances the formation rate of hydrocarbons with further stabilization at 8 wt%. The surface area of $BiVO_4$ is quite low and saturation of {010} facets takes place already at relatively low Cu content. Hydrogen production follows the same trend as hydrocarbon production and indicates on not full utilization of hydrogen for CO_2 reduction during photocatalysis. For other catalysts hydrogen production was also related to production of hydrocarbons.

Table 2. *Effect of Cu content on the performance of $CuO_x/BiVO_4$-0.20M for photocatalytic reduction CO_2 with H_2O*

Catalyst	Product formation rate (μmol g^{-1} h^{-1})							Hydrocarbon formation rate (μmol g^{-1} h^{-1})
	CO	CH_4	C_2H_6	C_3H_8	HCHO	CH_3OH	H_2	
1% $CuO_x/BiVO_4$	0.51	0.73	0	0	0	0	0	0.73
3% $CuO_x/BiVO_4$	0.82	2.5	0.61	0.42	0.35	0.55	0.42	4.4
5% $CuO_x/BiVO_4$	1.4	3.5	1.1	0.80	0.60	0.82	0.91	6.8
8% $CuO_x/BiVO_4$	1.3	3.3	1.0	0.63	0.51	0.60	0.96	6.0

The catalytic properties after deposition of co-catalysts by photo-oxidation over $CuO_x/BiVO_4$ have been studied by catalytic tests at the same conditions (**Figure 11**). The catalytic activity was gradually increasing in the row: $CuO_x/BiVO_4$<$MnO_x/CuO_x/BiVO_4$ <$PbO_2/CuO_x/BiVO_4$ <$CoO_x/CuO_x/BiVO_4$. It is interesting to note that deposition of co-catalysts does not lead to significant change in the selectivity to hydrocarbons (**Figure S3, SI**). Methane was still responsible for about 40 % of carbon utilization with selectivity about 20 % to ethane and propane and rest to heavier hydrocarbons. Afterwards the catalytic performance of $CoO_x/CuO_x/BiVO_4$ has been optimized by variation of CoO_x content. The catalytic behavior is similar to those of Cu with increase of the catalytic activity till 5 wt% of CoO_x and stable performance at higher loading (**Table S1, SI**). Thus, the highest catalytic activity for CO_2 reduction by water is achieved for the $CuO_x/CoO_x/BiVO_4$ catalyst with selective photo-

deposited CuO_x and CoO_x nanoparticles over {010} and {110} facets, respectively. For comparison, the $CuO_x/CoO_x/BiVO_4$ (imp) synthesized by impregnation method with non-selective loading of CuO_x and CoO_x demonstrates much lower catalytic activity and significantly higher contribution of methane in the products (**Figure 11, Figure S3, SI**). This result indicates that the photocatalytic performance can be significantly enhanced when the reduction/oxidation co-catalysts were selectively deposited on the corresponding reduction/oxidation reaction facets, which can minimize electron-hole pairs recombination. This assumption has been confirmed by the fact that intensity of photoluminescence band decreased significantly by loading CuO_x and CoO_x onto the $BiVO_4$-0.20M crystal (**Figure 5**).

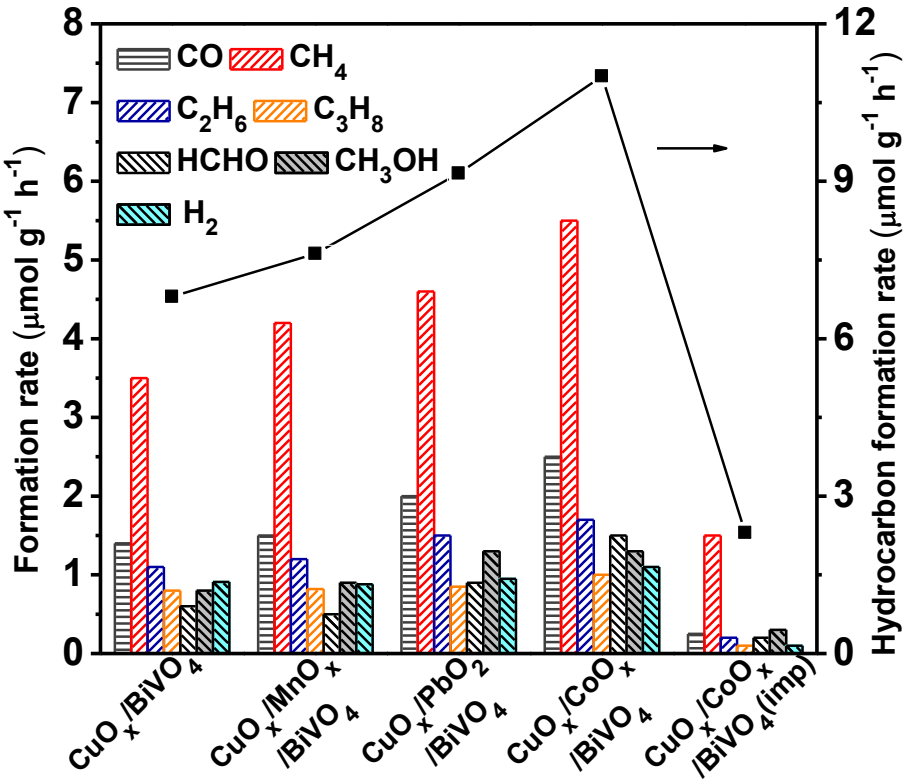

Figure 11. *Effect of cocatalyst on the performance of $CuO_x/BiVO_4$-0.20M for photocatalytic reduction CO_2 with H_2O.*

The stability of optimized catalyst containing 5 wt% Cu and 5 wt% Co over $BiVO_4$-0.20M has been studied by repeated tests with degassing and CO_2 reintroduction after 7 h of reaction. Similar activities for the formations rate of hydrocarbon fuels were observed after five cycles (**Figure 11**).

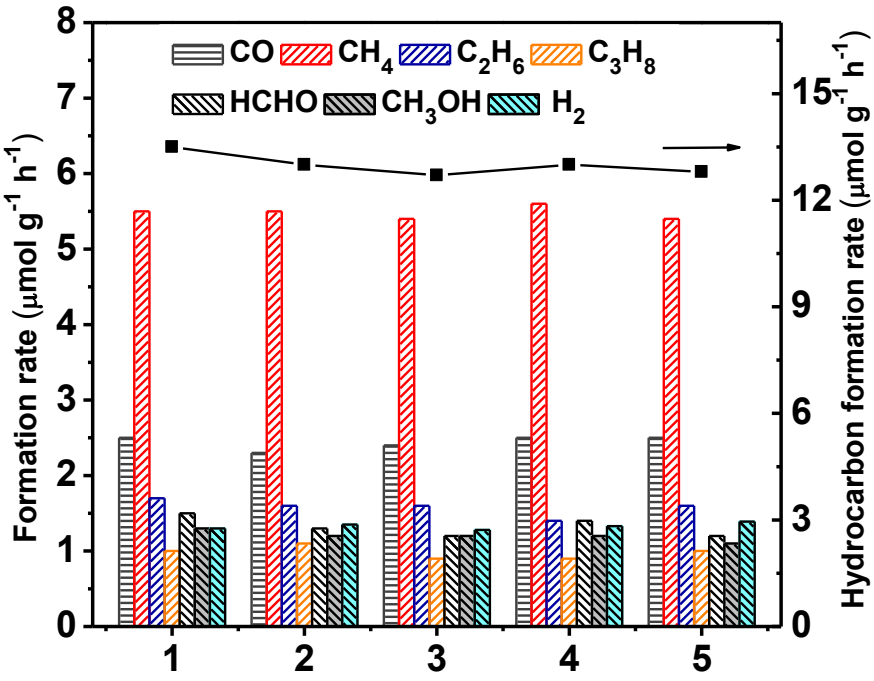

Figure 12. *Repeated uses of the 5 wt% CuO_x/5 wt% CoO_x /$BiVO_4$-0.20M catalyst for photocatalytic reduction of CO_2 with H_2O.*

Table 3 shows that the formation rate of the CO_2 reduction over CoO_x/CuO_x/$BiVO_4$ catalyst under visible light range (382-600 nm) is only slightly lower compared to the results with light range before filtration (240-600 nm). The main advantage of $BiVO_4$ as semiconductor in comparison with TiO_2 is its ability to work under visible light irradiation

Table 3. *Performances of the 5 wt% CuO_x/5 wt%CoO_x /$BiVO_4$-0.20 M catalyst for*

photocatalytic reduction CO_2 with H_2O measured under irradiation at different spectral ranges.

Spectral range of irradiation (nm)	Product formation rate (μmol g^{-1} h^{-1})[a]							Hydrocarbon formation rate (μmol g^{-1} h^{-1})
	CO	CH_4	C_2H_6	C_3H_8	HCHO	CH_3OH	H_2	
dark	0	0	0	0	0	0	0	0
240-600	1.5	3.8	1.1	0.50	1.1	0.81	1.0	7.3
382-600	0.60	2.0	0.52	0.21	0.30	0.41	0.2	3.1

[a] *Reaction conditions: catalyst, 0.1 g; Gas phase pressure, CO_2 0.2 Mpa; H_2O 15 mL; irradiation time, 7h; light source, Hamamatsu LC8-06 Hg-Xe stabilized irradiation lamps with a spectral irradiance in the range 240-600; Cut-off filter: visible light, 382 nm < λ < 600 nm.*

3.3 Z-scheme mechanism of the CuO_x/CoO_x /$BiVO_4$-0.20M catalyst for photocatalytic reduction CO_2 with H_2O

The valence band (VB) of Cu_2O is very close to the conduction band (CB) of $BiVO_4$. This fact suggests a possibility of construction of the Z-scheme photocatalysis system for reduction of CO_2 similar to the previous reports [34, 45-47]. The significant enhancement of photocatalytic CO_2 reduction can be explained by Z-scheme charge-transfer mechanism (**Figure 13**).

In summary, when both Cu_2O and $BiVO_4$ were excited by the irradiation, the photogenerated electrons in the CB of $BiVO_4$ recombine with the photogenerated holes in the VB of Cu_2O owing to their close band position. Finally, the photogenerated electrons in the

CB of Cu_2O are used for the reduction of CO_2 produce hydrocarbon fuels, while the photogenerated holes in the VB of $BiVO_4$ transfer to Co_3O_4 of oxidation co-catalyst, which used for the oxidation reaction of water (**Figure 13**).

The effect of close position of CB of $BiVO_4$ and VB of Cu_2O has been verified by deposition of other metal oxides (WO_x, FeO_x and ZnO) by photo-reduction technique with different band positions instead of CuO_x (**Figure 9**). The activity correlates well with band position on the **Figure 13**. Thus, FeO_x and WO_x almost did not affect catalytic activity of pure $BiVO_4$ due to low CB potential in comparison with the CO_2/CH_4 reduction potential. However, ZnO with higher reduction potential results in significant increase of the catalytic activity.

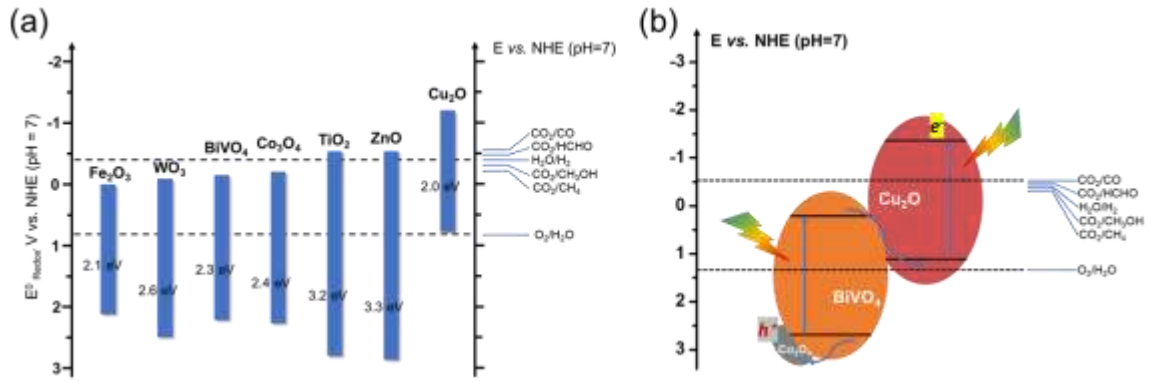

Figure 13. *(a) Comparison of the band structures of various semiconductor with respect to the redox potentials of reduction of CO_2, (b) Schematic of the Z-scheme of $CuO_x/CoO_x/BiVO_4$-0.20M catalyst.*

4. Conclusion

The present work focuses on the design efficient photocatalyst construction for the preferential photocatalytic reduction of CO_2 with H_2O. The monoclinic $BiVO_4$ crystals with truncated tetragonal bipyramidal morphology and controllable exposed {010} and {110} facets ratios have been synthesized. The fraction of {010} facets could be varied in the range from 26 to 75 %. The facet-selective photo-deposition of the metal oxides can significantly enhance the photocatalytic reduction of CO_2. $BiVO_4$ crystals containing 64% of {010} facets fraction with Cu_2O and Co_3O_4 nanoparticles photo-deposited onto {010} and {110} facets, respectively, were the most efficient for the separation of photogenerated electron-hole pairs. This catalyst demonstrated the highest stable catalytic activity toward production of hydrocarbons even under visible light irradiation. The construction of Z-scheme for CO_2 reduction by water using oxidation and reduction co-catalysts played a key role in enhancing of the efficiency of charge separation.

Keywords: photocatalysis; structural sensitivity; reduction of CO_2; bismuth vanadate; Z-scheme

References

[1] E. Worrell, L. Price, N. Martin, C. Hendriks, L.O. Meida, *Ann. Rev. Environ. Resour.* **2001**, 26, 303-329.
[2] J. Barber, *Chem. Soc. Rev.* **2009**, 38, 185-196.
[3] S. Xie, Q. Zhang, G. Liu, Y. Wang, *Chem. Commun.* **2016**, 52, 35-59.
[4] V.P. Indrakanti, J.D. Kubicki, H.H. Schobert, *Energy Environ. Sci.* **2009**, 2, 745-758.
[5] S.C. Roy, O.K. Varghese, M. Paulose, C.A. Grimes, *ACS Nano.* **2010**, 4, 1259-1278.
[6] A. Corma, H. Garcia, *J. Catal.* **2013**, 308, 168-175.
[7] S.N. Habisreutinger, L. Schmidt-Mende, J.K. Stolarczyk, *Angew. Chem. Int. Ed.* **2013**, 52, 7372-7408.
[8] L. Liu, H. Zhao, J.M. Andino, Y. Li, *ACS Catal.* **2012**, 2, 1817-1828.

[9] W. Jiao, L. Wang, G. Liu, G.Q. Lu, H.-M. Cheng, *ACS Catal.* **2012**, 2, 1854-1859.
[10] H.-a. Park, J.H. Choi, K.M. Choi, D.K. Lee, J.K. Kang, *J. Mater. Chem.* **2012**, 22, 5304-5307.
[11] H. Tsuneoka, K. Teramura, T. Shishido, T. Tanaka, *J. Phys. Chem. C* **2010**, 114, 8892-8898.
[12] Q. Liu, Y. Zhou, J. Kou, X. Chen, Z. Tian, J. Gao, S. Yan, Z. Zou, *J. Am. Chem. Soc.* **2010**, 132, 14385-14387.
[13] N. Zhang, S. Ouyang, P. Li, Y. Zhang, G. Xi, T. Kako, J. Ye, *Chem. Commun.* **2011**, 47, 2041-2043.
[14] X. Chen, Y. Zhou, Q. Liu, Z. Li, J. Liu, Z. Zou, *ACS Appl. Mater. Inter.* **2012**, 4, 3372-3377.
[15] H. Cheng, B. Huang, Y. Liu, Z. Wang, X. Qin, X. Zhang, Y. Dai, *Chem. Commun.* **2012**, 48, 9729-9731.
[16] N. Zhang, R. Ciriminna, M. Pagliaro, Y.-J. Xu, *Chem. Soc. Rev.* **2014**, 43, 5276-5287.
[17] X. Chen, S.S. Mao, *Chem. Rev.* **2007**, 107, 2891-2959.
[18] G. Liu, C.Y. Jimmy, G.Q.M. Lu, H.-M. Cheng, *Chem. Commun.* **2011**, 47, 6763-6783.
[19] Z.-F. Huang, L. Pan, J.-J. Zou, X. Zhang, L. Wang, *Nanoscale* **2014**, 6, 14044-14063.
[20] X. Han, Q. Kuang, M. Jin, Z. Xie, L. Zheng, *J. Am. Chem. Soc.* **2009**, 131, 3152-3153.
[21] J. Yu, J. Low, W. Xiao, P. Zhou, M. Jaroniec, *J. Am. Chem. Soc.* **2014**, 136, 8839-8842.
[22] G. Xi, J. Ye, *Chem. Commun.* **2010**, 46, 1893-1895.
[23] R. Li, F. Zhang, D. Wang, J. Yang, M. Li, J. Zhu, X. Zhou, H. Han, C. Li, *Nat. Commun.* **2013**, 4, 1432.
[24] S. Xie, Z. Shen, H. Zhang, J. Cheng, Q. Zhang, Y. Wang, *Catal. Sci. Technol.* **2017**, 7, 923-933.
[25] W.-C. Huang, L.-M. Lyu, Y.-C. Yang, M.H. Huang, *J. Am. Chem. Soc.* **2011**, 134, 1261-1267.
[26] L. Wang, J. Ge, A. Wang, M. Deng, X. Wang, S. Bai, R. Li, J. Jiang, Q. Zhang, Y. Luo, *Angew. Chem. Int. Ed.* **2014**, 126, 5207-5211.
[27] P. Li, Y. Zhou, Z. Zhao, Q. Xu, X. Wang, M. Xiao, Z. Zou, *J. Am. Chem. Soc.* **2015**, 137, 9547-9550.
[28] J. Ran, M. Jaroniec, S.Z. Qiao, *Adv. Mater.* **2018**, 30, 1704649.
[29] Y. Liu, B. Huang, Y. Dai, X. Zhang, X. Qin, M. Jiang, M.-H. Whangbo, *Catal. Commun.* **2019**, 11, 210-213.
[30] W. Dai, H. Xu, J. Yu, X. Hu, X. Luo, X. Tu, L. Yang, *Appl. Surf. Sci.* **2015**, 356, 173-180.
[31] P. Zhou, J. Yu, M. Jaroniec, *Adv. Mater.* **2014**, 26, 4920-4935.
[32] Z.-H. Wei, Y.-F. Wang, Y.-Y. Li, L. Zhang, H.-C. Yao, Z.-J. Li, *J. CO2 Util.* **2018**, 28 ,15-25.
[33] J.M. Sommers, N.P. Alderman, C.J. Viasus, S. Gambarotta, *Dalton T.* **2017**, 46, 6404-6408.
[34] C. Kim, K.M. Cho, A. Al-Saggaf, I. Gereige, H.-T. Jung, ACS *Catal.* **2018**, 8, 4170-4177.
[35] Y. Park, K.J. McDonald, K.-S. Choi, *Chem. Soc. Rev.* **2013**, 42, 2321-2337.
[36] X. Wang, Z. Feng, J. Shi, G. Jia, S. Shen, J. Zhou, C. Li, *PCCP* **2010**, 12, 7083-7090.
[37] J. Espinós, J. Morales, A. Barranco, A. Caballero, J. Holgado, A. González-Elipe, *J. Phys. Chem.* B **2002**, 106, 6921-6929.

[38]J.-Y. Park, Y.-S. Jung, J. Cho, W.-K. Choi, *Appl. Surf. Sci.* **2006**, 252, 5877-5891.
[39]T. Ghodselahi, M. Vesaghi, A. Shafiekhani, A. Baghizadeh, M. Lameii, *Appl. Surf. Sci.* **2008**, 255, 2730-2734.
[40]Q. Zhai, S. Xie, W. Fan, Q. Zhang, Y. Wang, W. Deng, Y. Wang, *Angew. Chem. Int. Ed.* **2013**, 125, 5888-5891.
[41]R. Riva, H. Miessner, R. Vitali, G. Del Piero, *Appl. Catal., A* **2000**, 196, 111-123.
[42]K. Qian, W. Huang, Z. Jiang, H. Sun, *J. Catal.* **2007**, 248, 137-141.
[43]C. Yuan, L. Yang, L. Hou, J. Li, Y. Sun, X. Zhang, L. Shen, X. Lu, S. Xiong, X.W. Lou, *Adv. Funct. Mater.* **2012**, 22, 2560-2566.
[44]T. Liu, X. Zhou, M. Dupuis, C. Li, *PCCP* **2015**, 17, 23503-23510.
[45]C. Zhou, S. Wang, Z. Zhao, Z. Shi, S. Yan, Z. Zou, *Adv. Funct. Mater.* **2018**, 180, 1214.
[46]Y. Deng, L. Tang, G. Zeng, C. Feng, H. Dong, J. Wang, H. Feng, Y. Liu, Y. Zhou, Y. Pang, Environ. Sci-Nano **2017**, 4, 1494-1511.
[47]M. Zhu, Z. Sun, M. Fujitsuka, T. Majima, *Angew. Chem. Int. Ed.* **2018**, 57, 2160-2164.